

Development of hybrid scaffolds with biodegradable polymer composites and bioactive hydrogels for bone tissue engineering

Yi-Ting Chen^a, Ya-Han Chuang^b, Chao-Ming Chen^c, Jir-You Wang^c, Jane Wang^{a,*}

^a Department of Chemical Engineering, National Tsing Hua University, Hsinchu 300044, Taiwan

^b Interdisciplinary Program of Life Science and Medicine, National Tsing Hua University, Hsinchu 300044, Taiwan

^c Department of Orthopedics Surgery and Traumatology, Taipei Veterans General Hospital, Taipei 11217, Taiwan

ARTICLE INFO

Keywords:

Tissue engineering
Bone regeneration
3D printing
Polymer composite

ABSTRACT

The development of treatments for critical-sized bone defects has been considered an important topic in the biomedical field because of the high demand for transplantable bone grafts. Following the concept of tissue engineering, implantation of biocompatible porous scaffolds carrying cells and regulating factors is the most efficient strategy to stimulate clinical bone regeneration. With the advancement in the development of 3D-printing techniques, scaffolds with highly controllable architectures can be fabricated to further improve healing efficacies. However, challenges such as the limited biocompatibility of resin materials and poor cell-carrying capacities still exist in the application of current scaffolds. In this study, a novel biodegradable polymer, poly(ethylene glycol)-co-poly(glycerol sebacate) acrylate (PEGSA), was synthesized and blended with hydroxyapatite (HAP) nanoparticles to produce osteoinductive and photocurable resins for 3D printing. The composites were optimized and applied in the fabrication of gyroid scaffolds with biomimetic characteristics and high permeability, followed by the combination of bioactive hydrogels containing Wharton's jelly-derived mesenchymal stem cells (WJMSC) to increase the efficiency of cell delivery. The promotion of osteogenesis from 3D-printed scaffolds was confirmed *in-vivo* while the hybrid scaffolds were proven to be great platforms for WJMSC culture and differentiation *in-vitro*. These results indicate that the proposed hybrid systems, combining osteoinductive 3D-printed scaffolds and cell-laden hydrogels, have great potential for bone tissue engineering and are expected to be applied in the treatment of bone defects based on active tissue regeneration.

1. Introduction

Bone tissue engineering (BTE) is an emerging field aimed at promoting the full recovery of bone defects using a combination of artificial extracellular matrix (ECM), cells and regulating factors that promote osteogenesis [1]. Synthetic ECM, which refers to scaffolds in most studies, is usually made into porous and interconnected structures with osteogenic biomaterials to provide a favorable microenvironment for cell adhesion and proliferation [2–4]. Recently, various 3D-printing technology have been applied to generate BTE scaffolds for fast prototyping, well-controlled microstructures, and customization [5–7]. Printing techniques based on stereolithography, such as digital light processing additive manufacturing (DLP-AM), are gaining attention because of their better printing resolution than that of common extrusion-based methods [8,9]. A wide variety of photocurable materials have been developed to produce BTE scaffolds via DLP-AM,

including cell-laden hydrogels [10], bioceramics [11] and biocompatible polymers [12]. Despite the specific advantages of these materials in different applications, few of them have led to the full *in-vitro* construction of scaffolds similar to autografts. Therefore, the design of materials and scaffolds is critical for fully reconstructing bone defects using scaffold-based tissue engineering.

Poly(glycerol sebacate) (PGS) is a biodegradable and biocompatible polyester that has been widely applied in tissue regeneration, including in the liver, cardiovascular system, and osteochondral system [13–15]. In the field of BTE, PGS has been applied as a basal scaffold material owing to its highly elastic and osteoconductive characteristics [16–18]. To further improve the biocompatibility, PGS has been combined with other polymers to generate a series of copolymers [19,20]. One of the examples: The incorporation of poly(ethylene glycol) (PEG) segments into the PGS backbone to synthesize PEGylated poly(glycerol sebacate) (PEGS) [21]. With the increased hydrophilicity contributed by PEG

* Corresponding author.

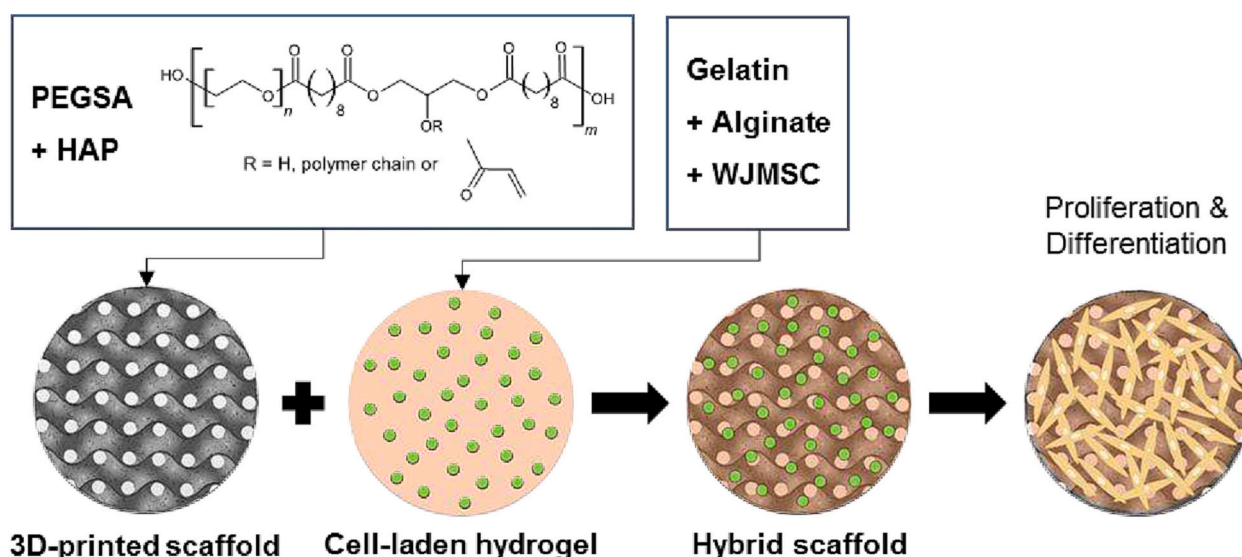
E-mail address: janewang@mx.nthu.edu.tw (J. Wang).

<https://doi.org/10.1016/j.bioadv.2023.213562>

Received 5 May 2023; Received in revised form 19 June 2023; Accepted 17 July 2023

Available online 23 July 2023

2772-9508/© 2023 Elsevier B.V. All rights reserved.



Scheme 1. The development process of hybrid scaffolds for BTE.

segments, the affinity for cell adhesion is further improved, leading to higher osteoconductivity while preserving most of the strengths of PGS. In previous studies, PEGS has been confirmed to hold great potential in promoting bone repair [22]. Despite the suitable properties of PEGS for bone regeneration, the morphologies of scaffolds made with these materials usually cannot be well controlled owing to limited options in the fabrication methods. Hence, improvements in the processability of PEGS through chemical modification are required for practical applications.

Bioceramics are commonly used as additives in polymeric materials for BTE because bone is naturally a combination of polymers and minerals [23]. Hydroxyapatite (HAP), the natural form of calcium phosphate mineral in bone tissue [24], is the most common bioceramic used in the fabrication of polymer composite scaffolds. HAP is highly osteoconductive and osteoinductive [25,26], and more recently, HAP has been used in the form of nanoparticles or microparticles to further increase its efficacy [27,28]. By blending HAP particles with polymers, composite scaffolds have been produced, integrating the advantages of both polymers and minerals.

Recently, cell-laden hydrogels have become an attractive form of cell delivery [29,30]. Natural polymers are often selected over synthetic polymers to prepare gels because of their similar physical and chemical properties to natural ECM. A well-known example is a hydrogel fabricated with alginate and gelatin [31], which combines the osteoinductive property of gelatin with the low toxicity and efficient gelation process of alginate, making them ideal cell carriers for BTE [32]. However, cell-laden hydrogels still face the challenges of insufficient mechanical strength and low durability owing to their highly swollen nature and rapid degradation. To overcome these problems, polymeric scaffolds have been combined with hydrogels by printing along with scaffolds [33] or directly injected into porous spaces [34]. With the combination of hydrogels and porous scaffolds, the stiffness of these hybrid constructs can be maintained while providing a larger surface area for cell proliferation.

In this study, hybrid scaffolds comprising 3D-printed constructs and cell-laden hydrogels were developed and characterized. Porous 3D scaffolds were fabricated with optimized polymer composites via DLP-AM, followed by integration of bioactive hydrogels to further improve the efficacy of the printed constructs. As demonstrated in Scheme 1, the resulting hybrid systems were characterized and proved to be excellent platforms for stem cell proliferation and differentiation. Overall, our design aims to provide new options with great potential for cell culture and delivery in BTE.

Table 1

Theoretical and experimental concentration of acrylate groups.

Sample code	Theoretical molar ratio (glycerol : AC)	Theoretical concentration of acrylate group (mmol/g)	Experimental molar ratio (glycerol : AC)	Experimental concentration of acrylate group (mmol/g)
P40	1 : 1.2	2.42	1 : 0.83	2.01
P50	1 : 1.2	1.86	1 : 0.79	1.47
P60	1 : 1.2	1.26	1 : 0.67	0.84

2. Materials and methods

2.1. Materials

Sebacic acid (99 %), PEG ($M_w = 1000$ g/mol), glycerol (99 %), triethylamine (99.5 %), acryloyl chloride (97 %), hydroxyapatite powder and nanopowder (<200 nm), diphenyl(2,4,6-trimethylbenzoyl) phosphine oxide (TPO, 97 %), Sudan Black B, sodium alginate, gelatin, calcium chloride (97 %), sodium citrate (99 %), and pNPP Phosphatase Assay kit were purchased from Sigma-Aldrich. Fetal bovine serum, DMEM, OGM, bFGF, Prestoblu reagent, CCK-8 reagent, and the PicoGreen dsDNA Assay Kit were purchased from Thermo Fisher Scientific. DMP1 primary antibody and fluorescent secondary antibody were purchased from Arigo Biolaboratories. All the reagents were used without further purification. All data were obtained from at least three independent experiments.

2.2. Hybrid scaffold preparation

2.2.1. Synthesis of PEGSA

The PEGS synthesis was divided into two steps, as reported previously [21] (Fig. S1a). PEG and sebacic acid (SAA) were mixed at 130 °C under nitrogen for 1 h, followed by the reaction at 40 Pa for 24 h to generate a linear SAA-PEG pre-polymer. Glycerol was added, and the reaction was allowed to proceed for 48 h to synthesize PEGS. The molar ratio of (PEG + glycerol) to SAA was maintained at 1:1, while the weight ratio of PEG was tuned from 40 to 60 %. The resulting polymers were named PEGS40, PEGS50, and PEGS60, respectively.

Next, the PEGS polymer was reacted with acryloyl chloride (AC) to produce PEGSA (Fig. S1b). The molar ratio of AC to glycerol was set to 1:1.2 to maximize the degree of acrylation (Table 1). PEGS polymer and 4-dimethylaminopyridine were dissolved in dichloromethane (DCM) at

Table 2

Theoretical characteristics of gyroid scaffolds.

Sample code	Diameter (mm)	Height (mm)	Porosity (%)	Pore size (μm)	Wall thickness (μm)
G200	6	2	95.20	260	20
G300	6	2	94.70	360	30
G400	6	2	95.00	510	50

room temperature under nitrogen and mixed until the mixture became homogeneous. The mixture was then cooled to 0 °C in an ice bath. Triethylamine was quickly injected into the mixture, followed by a slow and steady injection of AC. After the injections, the ice bath was removed and the reaction continued at room temperature. After 24 h, DCM was removed by rotary evaporation and ethyl acetate was added to dissolve PEGSA. The salt generated during the reaction was removed via suction filtration. To remove excess TEA by co-vaporization, deionized water was added and removed using a rotary evaporator. The resulting products were named P40, P50, and P60 according to their polymer backbones. The yield of all PEGSA synthesis was around 98 %, calculated by dividing the weight of collected products by the theoretical weight of synthesized products.

2.2.2. Fabrication of PEGSA and polymer composite films

HAP micro-(<50 μm) or nanoparticles (<200 nm) were mixed with 99 % ethanol to prepare a 20 wt% solution. The solution was sonicated for 30 min before being mixed with PEGSA. The final weight ratio between the PEGSAs and HAP particles was fixed at 3:1. Subsequently, ethanol was removed using a rotary evaporator. Photoinitiator TPO and 99 % ethanol were added to achieve 2 % and 5 %, respectively. The prepared materials were homogenized, poured into molds made of stainless steel, and crosslinked in a 405 nm LED box. The thickness of the molds was 0.5 mm and the length of light exposure was 30 s per side. The mold thickness and light exposure time were doubled during the fabrication of the samples used in the compression test. The fabrication of pure PEGSA films followed similar procedures. After the curing process, the films were cut off from the molds and soaked in 95 % w ethanol for one day. Subsequently, the films were washed with decreasing concentrations of ethanol solution (75 %, 50 %, 25 %) with the time of 1 h at each concentration. Finally, the films were soaked in water for one day. The resulting composite materials prepared with HAP microparticles were named HP40, HP50 and HP60 according to the PEG content of added PEGSAs, while similar rules were applied for the ones prepared with HAP nanoparticles, naming nHP40, nHP50 and nHP60 respectively.

2.2.3. Design and fabrication of 3D-printed scaffolds

The design is summarized in Table 2. Basic structures were constructed using *MathMod* followed by conversion into 3D meshes using *MeshLab*. *Imageware* was used to tune the size of the 3D models. The 3D models without volume were solidified in *Blender* with specific wall thicknesses for each design. In this step, the edges were cut to ensure isotropic characteristics. The uncrosslinked polymer composites were prepared as previously described. 0.04 wt% Sudan Black B was added to the composites to increase the printing resolution. Gyroid scaffolds were fabricated using a DLP printer (built by the Cheng lab at the National Taiwan University of Science and Technology). The exposure time for the first layer was 3.6 s while the curing time for all the other layers was 2.4 s. The ink was renewed every 20 layers during printing. The printed products were peeled off from the platform and soaked in 95 % ethanol, followed by sonication for 30 min to remove the uncrosslinked composites stuck within the pores.

2.2.4. Fabrication of cell-laden hydrogel

The 15 wt% gelatin stock solution was prepared by dissolving gelatin

powder in phosphate buffer saline (PBS) and the resulting solution was sterilized by autoclave. 1 wt% alginate solution in DI water was sterilized by 0.22 μm syringe filters. Sterile alginate solution was freeze-dried to obtain sterile alginate. The alginate solution was prepared by dissolving sterile alginate in PBS. The uncrosslinked hydrogels were prepared by mixing gelatin stock solution, alginate stock solution, and DMEM. The alginate concentration was fixed at 2 wt% while the gelatin concentration was set at 5, 6 or 7 wt% for AG5, AG6 and AG7 respectively. To prepare the cell-laden hydrogel, the cells were added to the hydrogel at a density of 600,000 cells/mL. The uncrosslinked cell-laden hydrogel was then injected directly into well plates or scaffolds, depending on the application. The gels were cooled in 4 °C fridge for 30 min to fix the shape before crosslinking in 300 mM CaCl₂ aqueous solution for 30 min. The crosslinked hydrogels were washed with DMEM for 3 times and cultured under normal cell conditions.

2.2.5. Fabrication of hybrid scaffolds

To eliminate autofluorescence, the 3D-printed scaffolds were soaked in 0.04 wt% Sudan Black B (SBB) solution in 70 % ethanol. After 24 h, the scaffolds were washed in DI water three times for 30 min each. The scaffolds were soaked overnight in DMEM before cell seeding. The uncrosslinked cell-laden hydrogels were injected into the scaffolds at approximately 50–70 μL/sample. After checking that all pores were filled, the hydrogel outside the scaffolds was gently removed. The scaffolds combined with gels were crosslinked, as mentioned in the previous section, generating hG200, hG300, and hG400 according to the pore sizes. After gelation, the gel scaffolds were transferred to 48-well plates and cultured under standard conditions. The culture medium was replaced every two days.

2.3. Physiochemical characterization

2.3.1. Chemical and physical characterization

The molecular weight of the PEGS copolymer was determined by gel permeation chromatography (GPC) using an Agilent HPLC column (ZORBAX 80 Å, 3 × 150 mm, 3.5 μm), with THF as the mobile phase. Fourier transform infrared (FT-IR) spectroscopy (NICOLET iS50, Thermo Scientific) was used to confirm the molecular structures. Nuclear magnetic resonance (¹H NMR) spectra were recorded on a VNMR-700 NMR spectrometer (with d-CHCl₃). The size of the wet scaffolds was recorded by bright-field imaging and calculated using *ImageJ*. The dry scaffolds were imaged using an electron microscope (JEOL JSM-5600, USA) at a voltage of 5 kV. EDX mapping for calcium was conducted with the same SEM system. The pore size is defined as the diameter of the circular void space observed from the top view.

2.3.2. Mechanical properties

All samples were first soaked in DI water for one day, and the solid films were cut into cylinders with a diameter of 6 mm. The compressive properties were measured by TA-ElectroForce with a 225 N load cell at a strain rate of 0.01 mm/s. Compression of the samples was maintained until the detection limits were reached. The stress-strain curves were recorded throughout the experiments. Compressive moduli were calculated from the linear region (~5 % strain) of the stress-strain curve.

2.3.3. Hydrophilicity properties

PEGSA and the composite films were soaked in DI water until fully swollen and cut into cylinders with a diameter of 15.5 mm. Water contact angles were measured using a SEO PHOENIX-1 contact angle analyzer. For swelling ratio measurements, the cylinders were dried in 50 °C oven for 1 d and weighed before and after soaking in DI water for 1 d. Swelling ratios were calculated by dividing the weights of the dry samples by the weights in the swollen state.

2.3.4. Hydrolysis degradation test

The sample preparation was the same as that described for the

hydrophilicity measurements. After soaking in DI water for 1 d, the sample was placed into 6-well plates with 10 mL of 0.1 M sodium hydroxide filled in each well. The plates were then placed in a 37 °C incubator for degradation. Degraded samples were collected every 2 h and the entire experiment lasted 8 h. The collected samples were washed with DI water to remove the degraded products. For samples that could not be moved with tweezers, filter papers and suction filtration were used to collect the samples. The samples were then dried in a 50 °C oven for 1 d before weighing. The percentage of the remaining mass was calculated by dividing the weights after degradation by the original weights.

2.3.5. Porosity measurements

The porosities were calculated based on the composite density of the solid control samples, which were printed with identical settings for scaffold fabrication. The sizes of the control samples were set to be the same as those of the porous samples. The solid cylinders were weighed and their sizes were measured using a Vernier caliper. The reference density of 3D printed composite was calculated using the measured volume and weight. A similar process was performed on the porous scaffolds to obtain their diameters, heights, and weights. The total volumes of the gyroid scaffolds, including the pores, could be calculated, while the solid volumes without pores could be estimated through the scaffold weight and reference density. Porosity was calculated using the following equation:

$$\text{Porosity} = \left(1 - \frac{\text{Volume of scaffold without pores}}{\text{Volume of scaffold including pores}}\right) \times 100\%$$

$$\text{Volume of scaffold without pores} = \frac{\text{Weight of scaffold}}{\text{Reference density}}$$

2.4. Biological characterization

2.4.1. Cell culture and seeding

Human umbilical cord Wharton's jelly mesenchymal stem cells (WJMSC) with passage numbers ranging from 4–7 were used in this study for biological experiments. Cells were cultured in low-glucose Dulbecco's Modified Eagle Medium (DMEM) supplemented with 20 % fetal bovine serum, 1.6 % penicillin-streptomycin (10,000 U/mL), and 4 ng/mL of human bFGF recombinant protein. For regular preparation of cells for experiments, the medium was replaced every 2–3 days. Passage of Cells were passaged at 90 % confluence at a subculture ratio of 1:4. All cell cultures were maintained at the 37 °C incubator with 5 % CO₂.

Before cell seeding, polymer films and 3D-printed scaffolds were sterilized in 70 % ethanol overnight. Next, samples were sequentially soaked in decreasing concentrations of ethanol solution (75 %, 50 %, 25 %) and DI water with the time of 1 h for each soaking step. The resulting samples were soaked overnight in the culture medium before cell seeding. Seeding density and culture conditions were set according to different experimental requirements, as described in the following sections.

2.4.2. Cytotoxicity and cell viability test

For cytotoxicity tests of the extracts based on ISO 10993-5, wet PEGSA and composite films were first cut into cylinders with a diameter of 6 mm and moved into 96-well plates. The medium (100 µL) was added to each well to prepare the extract. Polystyrene (PS) wells were used as positive controls for the viability calculations. At the same time, WJMSCs were seeded in 96-well plates with the density of 10,000 cells/well. After 24 h, the medium for the cells was replaced with extraction medium. The cells were then cultured for 24 h and viability was measured using the *PrestoBlue* assay following the manufacturer's instructions. The viability of the experimental groups was then calculated by dividing the absorbance of the experimental groups by the average absorbance of the PS groups.

For direct culture on the cylindrical films, cells were seeded on the surface of the films by adding 200 µL of the cell suspension at a density of 30,000 cells/mL. The medium was replaced every 2 days and cell viability was tested by the *PrestoBlue* assay on days 1 and 4. For the viability test of cell-laden hydrogels, samples were first fabricated into cylinders with 30 µL, and the viabilities were quantified by the CCK-8 assay according to the manufacturer's instructions on days 1, 4, and 7. In the hybrid scaffold section, control groups were prepared by direct cell seeding on scaffolds in 48-well plates. A cell suspension (400 µL) with a density of 120,000 cells/mL was added to each well. The experimental groups were prepared as previously described. Cell viability was measured using the CCK-8 assay on days 1, 4, 7, 14, and 21.

2.4.3. Live/dead cell imaging

The samples for live/dead cell imaging were fabricated by extruding 30 µL of the cell-laden hydrogels directly onto well plates. The hydrogels were soaked in 4 µM calcein-AM for 30 min at 37 °C or in 3.75 µM propidium iodide for 20 min at room temperature to label live cells and dead cells, respectively. The staining results were recorded using a fluorescence microscope (Nexcope NIB410) and analyzed using a Bio-Film Analyzer [35]. Viability was calculated by dividing the average area of dead cells by the average area of total cells. For the visualization of cells seeded on the scaffolds, the scaffolds were stained under the same conditions as mentioned above for live cell labelling.

2.4.4. ALP activity assay

To quantify the osteoinductive properties of the hybrid scaffolds, the cells were cultured in hybrid scaffolds, as previously described. The control group was prepared by direct seeding in 48 well plates at 48,000 cells/well. The samples were washed with PBS and transferred to a microtube on days 7 and 14. Sodium citrate (55 mM) was added to dissolve the hydrogel, followed by centrifugation at 3000 RPM to collect the cells. 1 % Triton aqueous solution was then added to release the ALP enzyme. After removing the scaffolds, the sample solutions underwent three freeze-thaw cycles at 37 °C and –20 °C. DNA concentration was quantified using the Quant-iT™ PicoGreen™ dsDNA Assay Kit according to the manufacturer's instructions. To test ALP enzymatic activity, para-nitrophenyl phosphate (pNPP) was added to the sample solutions, and the substrate conversion was measured by optical density at 405 nm. After subtracting the results from the reference O.D. 650, the final ALP activity data were obtained by dividing the OD values by the DNA concentrations.

2.4.5. Immunohistochemistry and quantification

Samples for immunohistochemical staining were prepared as previously described. The hybrid scaffolds were fixed with 10 % formaldehyde in TBS for 1 h, followed by permeabilization and blocking with 5 % FBS in 2 % Triton at 4 °C overnight. Goat-anti-human DMP1 was diluted 200-fold, according to the manufacturer's instructions, and added to the samples. After incubation at 4 °C overnight, the samples were incubated with 100-fold Donkey-anti-goat IgG (TRITC conjugated) diluted in 5 % FBS for 60 min at room temperature. DAPI solution was added to visualize nuclei. Imaging was performed immediately after the entire staining process using a fluorescence microscope (Nexcope NIB410). *BioFilmAnalyzer* was used to calculate the area ratio of the DMP1 signal, which was obtained by dividing the pixel number of the DMP1 channel by the pixel number of the DAPI channel.

2.4.6. In-vivo experiments

G200 and G400 scaffolds were prepared and sterilized as described above. All scaffolds were soaked in PBS before implantation. A critical-sized defect was created in the central parietal bone of each 8-week old male rat (Sprague Dawley; National Laboratory Animal Center, Taipei, Taiwan) under general anesthesia by administering Zoletil and Rompun. The defects (5 mm in diameter) were created using a trephine bur under saline irrigation. For the experimental groups, scaffolds were implanted

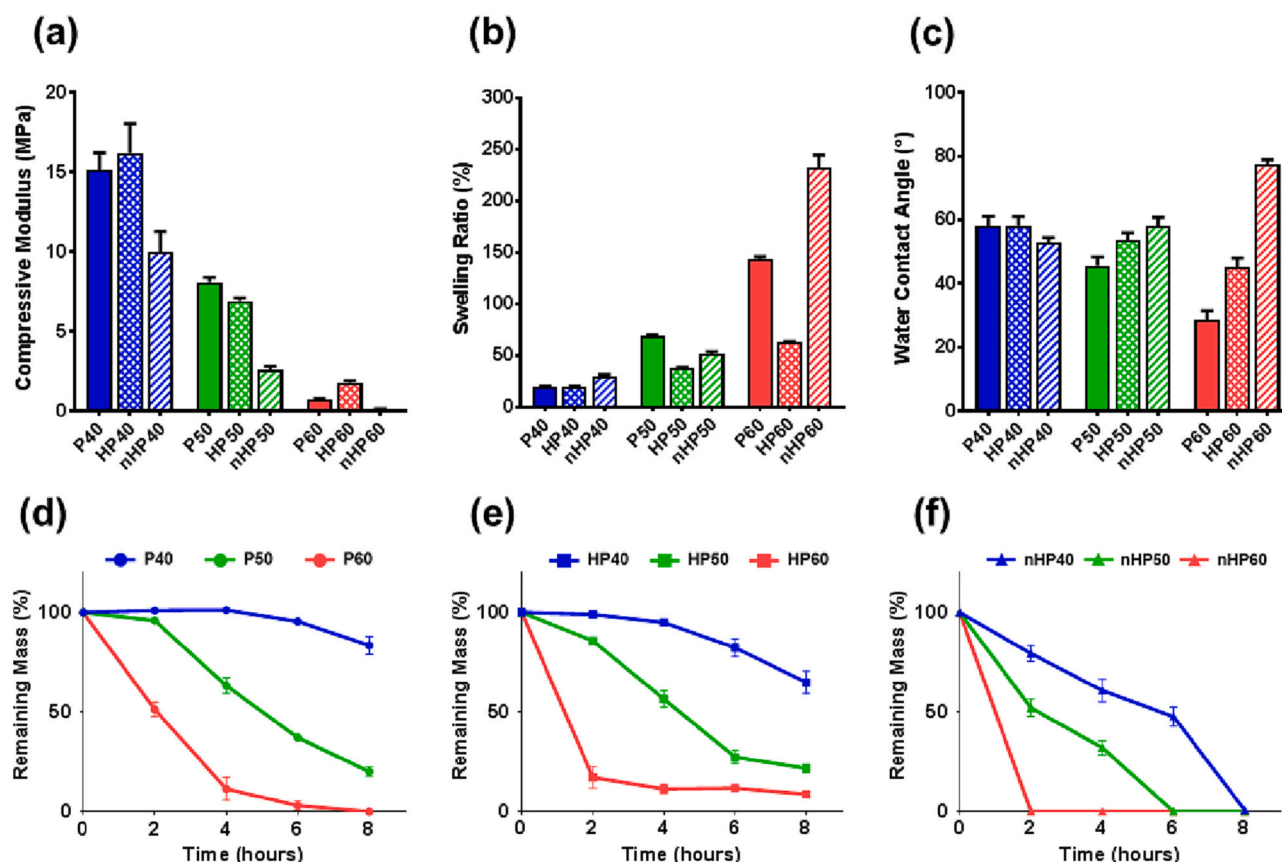


Fig. 1. Physical characterizations on composites including compression test (a), swelling ratio test (b), contact angle measurement (c) and hydrolysis degradation test (d–f).

immediately after defect creation, whereas the defects of the control groups were left untreated ($n = 3$ for each group). Recovery of locomotion was confirmed before subsequent animal maintenance. All *in vivo* experimental procedures in this study were reviewed and approved by the Institutional Animal Welfare Guidelines of Taipei Veterans General Hospital.

μ -CT scanning by Milabs U-CT^{HR} (resolution: 10 μ m) was applied to live rats at weeks 4 and 8 after surgery. The new bone volume ratio (BV/TV) and relative bone density were directly calculated from the reconstructed 3D files using ITK-SNAP and ImageJ. A cylindrical region (ϕ 5 mm \times 2 mm depth) within the defect was set as the volume of interest (VOI). BV/TV was defined as the new bone volume percentage in the VOI, while the relative bone density was calculated by dividing the intensity of voxels in the VOI with that of the surrounding native bone. All animals were sacrificed after being maintained for 8 weeks. Calvarial samples were then retrieved and decalcified for histological analysis. The sections were then embedded in paraffin. Sections were stained with hematoxylin–eosin (H&E) and Masson's trichrome (MT). The stained cells were imaged using an optical microscope, as described previously. New bone ratio in histological experiments were defined as the ratio of new bone areas in total defected area, which were calculated from MT images by ImageJ.

3. Results and discussion

3.1. Synthesis and characterization of PEGSA prepolymers

PEGs were first synthesized as polymer backbones and then chemically modified with acrylate groups to generate PEGSA as the main component in the photocurable resin. As reported previously by A. Patel et al., PEGs with PEG content ranging from 40 to 60 % was better

material for cell culture compared to the ones with other weight ratios [21]. Hence, the PEG content of PEGs was set to 40–60 % in this study. The molecular weight and polydispersity index (PDI) of the synthesized PEGs were measured using GPC, as shown in Table S1. All copolymers had a M_n of 4000 ± 400 Da, with PDI ranging from 1.37 to 1.60. For the incorporation of the acrylate group, the ratio between glycerol and acryloyl chloride (AC) was set at 1:1.2, to maximize the substitution of the hydroxyl groups (Table 1).

In the ^1H NMR spectra (Fig. S2a–b), the protons of methylene groups on sebacic acid contributed to the peaks at 1.25 ppm, 1.58 ppm and 2.28 ppm while the peaks from 4.08 to 4.16 ppm and 5.10–5.25 ppm were assigned to the protons of glycerol. The peaks at 3.66 ppm were observed from the methylene protons of PEG, indicating the incorporation of PEG segment. In addition, the acrylation of PEGs was confirmed by the peaks assigned to the alkenyl hydrogens of acrylate groups at 5.86 ppm, 6.12 ppm and 6.24 ppm (Fig. S2b). In the FT-IR spectra, a strong absorption band was found at 1740 cm^{-1} and a broad band at 3450 cm^{-1} , corresponding to carbonyl groups ($\text{C}=\text{O}$ stretch) from ester group and hydroxyl groups ($-\text{OH}$ stretch) respectively (Fig. S2b). In the spectrum of P40, the absorption band at 1640 cm^{-1} was an indication of the addition of acrylate group through the $\text{C}=\text{C}$ stretching, meanwhile, the stretching at 3450 cm^{-1} pointed toward the $-\text{OH}$ groups on PEGs backbone. With the addition of acrylate groups, it was clear that besides the appearance of $\text{C}=\text{C}$ stretching, the 3450 cm^{-1} band also decreased in signal intensity. Similar observation could be made from the NMR and FTIR spectra of the polymers with different PEG ratio (Fig. S3–4), proving the successful synthesis of PEGs and PEGSA.

To quantify the substitution of hydroxyl groups under different PEG ratio, the degree of acrylation was calculated by comparing the integrals of the peaks at 1.58 ppm (position “b”) and 6.12 ppm (position “h”) in

the ^1H NMR spectra of PEGSAs (Fig. S2b). The concentration of acrylate groups within the polymer matrix was then calculated (Table 1). With fewer glycerol molecules within the polymer backbones, it was expected that a higher PEG content would result in a lower concentration of acrylate groups. The results showed that more PEG led to a lower degree of acrylation, resulting in an even lower acrylate group concentration. This phenomenon can be explained by the formation of more PGS oligomers in the PEGS matrix with fewer incorporated PEG segments. In the second step of the PEGS synthesis (Fig. S1a), the SAA-PEG prepolymer, glycerol, and the remaining sebacic acid were all involved in the polycondensation reaction, providing the opportunity for the formation of a pure PGS chain. Since the amounts of glycerol and sebacic acid in PEGS40 synthesis were far greater than others, the chance to produce PGS oligomers was far greater than that for the formation of other polymers. These PGS chains were more reactive than PEGS, increasing the overall acrylation efficiency.

3.2. Material selection for 3D-printed BTE scaffolds

To prepare a 3D-printing resin with photocrosslinking ability and sufficient osteoinductivity, polymer composites were fabricated by adding HAP particles to PEGSA polymer matrices. The weight ratio of PEGSA to HAP was set at 3:1 to ensure sufficient photocrosslinking ability and osteoinductivity. The PEG weight ratio and HAP particle size were set as the variables in the composite formula. The PEG content was the key factor in the determination of crosslinking density and hydrophilicity, while the HAP particle size could affect the efficiencies of photocuring and mineral encapsulation. To select the most suitable formula for BTE, its physical properties, biocompatibility, and printing qualities were tested and discussed.

3.2.1. Physical properties

Compressive modulus, hydrophilicity properties, and degradation profile of the polymer composites were measured to determine the essential physical properties. As shown in Fig. 1, the PEG weight ratio and size of the HAP particles contribute differently to each physical property. More PEG was assumed to result in better hydrophilicity and lower crosslinking density, because PEG is a highly hydrophilic polymer that determines the acrylate group concentration. Moreover, there was a correlation between the degradation rate and material hydrophilicity. As the PEG content increased, a weaker compressive modulus, higher swelling ratio, smaller water contact angle, and faster degradation were observed (Fig. 1a–f). On the other hand, different effects from the addition of HAP were observed between the microcomposites and nanocomposites. After combining PEGSA with microparticles, it was observed that the degradation rate and mechanical properties remained roughly the same, while the incorporation of nanoparticles obviously decreased the compressive modulus and accelerated degradation (Fig. 1a, d, f). In the hydrophilicity measurements, differences between PEGSA and the polymer composites were only observed for materials with higher PEG contents. The addition of microparticles led to a lower swelling ratio, whereas the opposite trend was observed for the nanocomposites (Fig. 1b). As for the contact angle, both particles increased in number, and the effect was stronger for the composites with nanoparticles.

The addition of HAP, which resulted in opaque materials, may lower the photocuring efficiency, leading to a lower PEGSA crosslinking density. This light-blocking effect could be more severe for nanoparticles because of their larger surface areas. In addition, the nanoparticles were more efficient in separating the polymer chains, leading to even fewer crosslinks. As a result, the mechanical properties of the nanocomposites were weaker, and their degradation rates were faster than those of the pure polymers. Another possible situation for the composites is particle loss during the washing process. The water absorption ability of HAP is rather limited; therefore, it was expected that the composites containing HAP may present a lower swelling ratio, explaining the few cases in

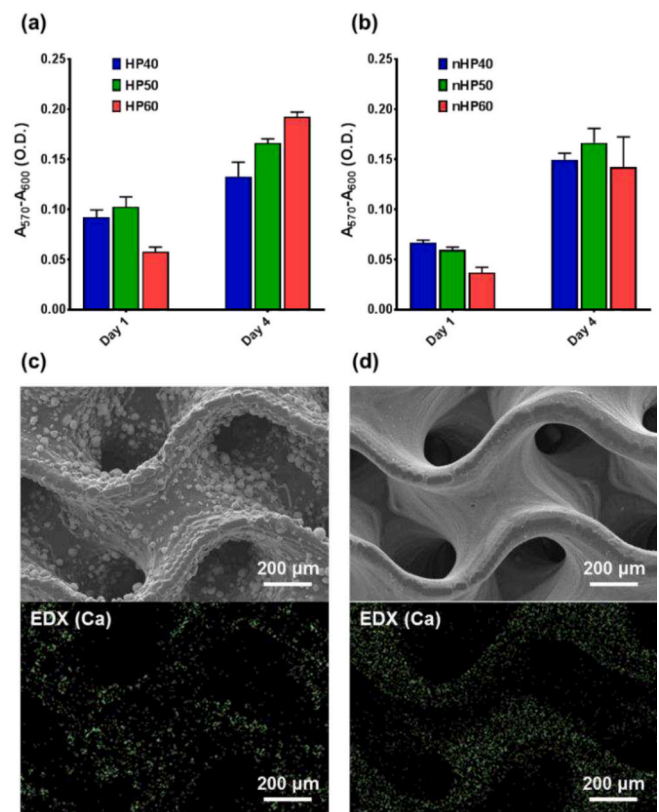


Fig. 2. Cell viability on composite materials (a–b) and printing test with HP40 (c) or nHP40 (d), demonstrated by both SEM and EDX (Ca) images.

which the water uptake decreased. On the other hand, when particles were lost, empty spaces could be filled during swelling, leading to a larger swelling ratio. Such an effect could be even more severe for cases with nanoparticles, as smaller particles are easier to flush away. However, the discussion above cannot be attributed to the observation in the contact angle tests. Studies have shown that the contact angle of pure HAP minerals is only approximately 10° [36]; therefore, the contact angle of polymer composites should decrease upon the addition of HAP. A possible reason for this is that more PGS segments were exposed on the surface with the addition of HAP, which decreased surface wettability. This was supported by the work of Zhang et al., who showed that for copolymers containing both hydrophilic and hydrophobic segments, microphase separation could occur during or after scaffold fabrication [37]. The addition of HAP may facilitate this process because some of the particles act as seeds for the nucleation of PEG crystallization. Once more PEG segments formed crystals with HAP, it was expected that the interaction between water and PEG would become weaker, leading to an increase in the contact angle. Moreover, this phenomenon could be more significant for nanocomposites because smaller particles lead to a higher nucleation efficiency. Nevertheless, the aforementioned conditions did not affect the successful fabrication of BTE materials. The compressive moduli of all composites reached the minimum requirement for inducing osteogenesis (>40 kPa) [38] and most contact angles were within a suitable range for cell adhesion and proliferation ($55\text{--}75^\circ$) [39]. For the selection of the composite formula, materials fabricated with PEGS40 and nanoparticles were considered more favorable than the others because of their significantly higher compressive moduli and faster degradation rates. Further characterization should be performed to determine the final formula for the 3D-printing resin.

3.2.2. Biocompatibility

To evaluate the biocompatibility of the candidate materials,

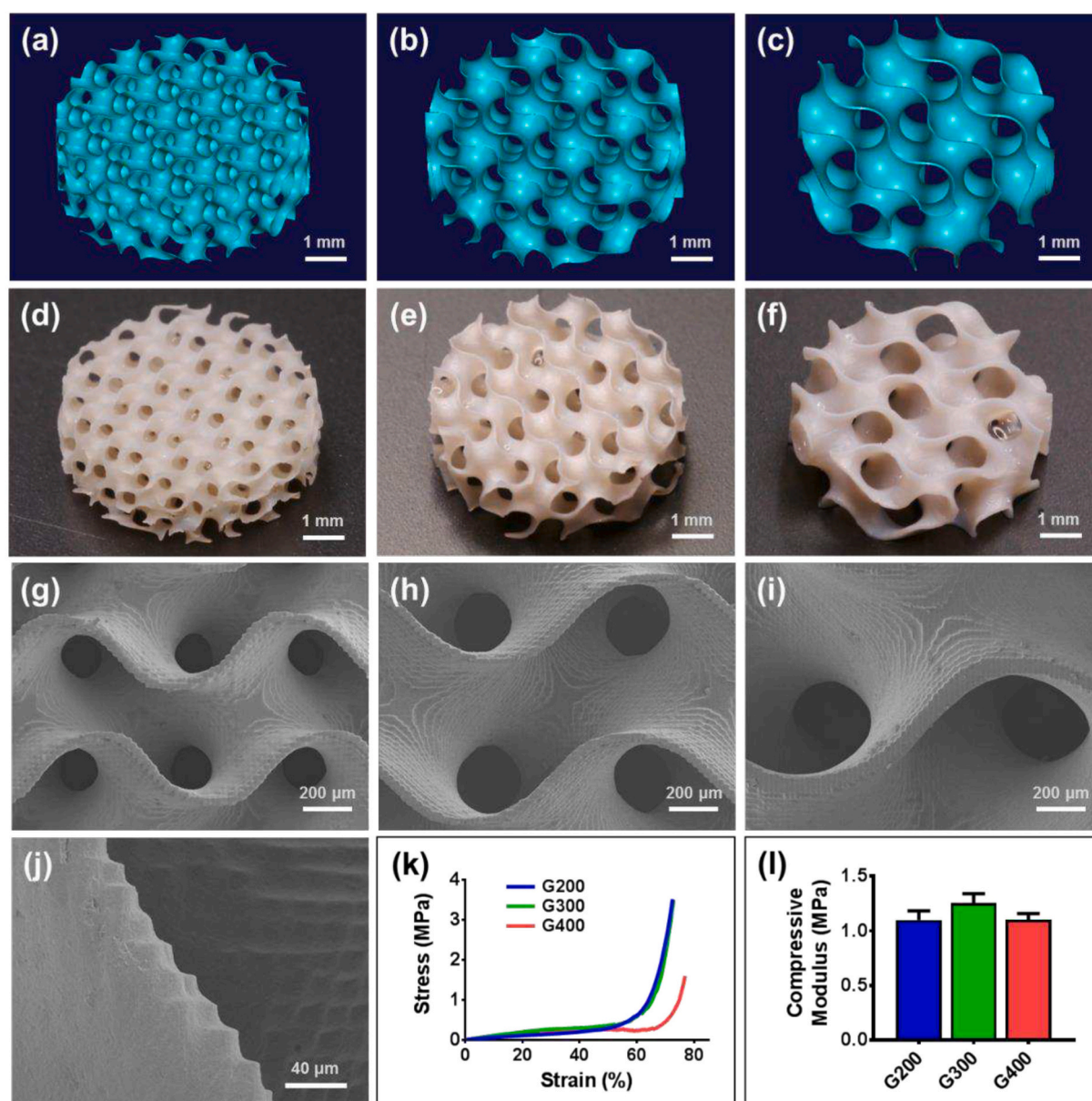


Fig. 3. Design and characterization of 3D-printed G200 (a, d, g, j), G300 (b, e, h) and G400 (c, f, i) including digital design (a–c), optical imaging (d–e), SEM (g–j) and compression tests (k–l).

cytotoxicity tests and direct cell culture of the films were conducted. In this study, Wharton's jelly-derived mesenchymal stem cells (WJMSC) were used as the test target. These cells have been proven to hold great potential in BTE due to their similar osteogenic potential compared to bone marrow-derived mesenchymal stem cells [40] but less immunogenicity in autograft and allogeneic transplantation [41]. Cytotoxicity tests were first performed on the extracts prepared with the PEGSAs and polymer composites. In the result of cytotoxicity test, the viability of cells cultured in PEGSA extracts increased with PEG content (Fig. S5). Since common sources of toxicity came from the byproducts or remaining reagents from the acrylation process, polymers with more PEG was less toxic for cells because less chemical reagents were added in the synthesis. In contrast, the cell viability of composite groups all maintained around 100 % (Fig. S5b, c). Possible explanations for this phenomenon was that the remaining toxic chemicals were washed out more efficiently in the cases of polymer composites due to their increased hydrophilicity compared to pure PEGSAs. Nevertheless, the viability of cells treated with the extracts was all above 70 % compared

to polystyrene control group, which reached the safety standard of biomaterials as ISO 10993-5 indicated [42].

To test the potential for cell proliferation on material surfaces, stem cells were directly seeded and cultured on the composites. The cell viability at days 1 and 4 was quantified using the *PrestoBlue* assay (Fig. 2a–b). The viability of cells on all composites increased from days 1 to 4, confirming the feasibility of the materials in promoting cell adhesion and proliferation. It was also observed that the viability of cells cultured on HP60 and nHP60 was clearly lower on day 1 than that of cells cultured on other PEG ratios, indicating fewer initial cell attachments. The poorer cell-material interactions could be explained by two factors: surface wettability and mechanical strength. Because appropriate surface wettability is necessary for cell adhesion, HP60 and nHP60, with contact angles relatively far from the suitable range, were expected to form weaker connections with the cells. In addition, the mechanical properties play an important role in triggering the function of adhesive proteins on cell membranes. It has been reported that stiffer surfaces usually lead to more stable cell adhesion [43] thus, the low

Table 3
Experimental characteristics of gyroid scaffolds.

Sample code	Diameter (mm)	Height (mm)	Porosity (%)	Pore size (μm)	Wall thickness (μm)
G200	5.92 ± 0.04	2.00 ± 0.02	82.44 ± 1.22	205.1 ± 10.3	47.05 ± 1.77
G300	5.90 ± 0.03	2.03 ± 0.03	83.44 ± 1.29	303.2 ± 14.5	45.29 ± 2.12
G400	5.91 ± 0.03	2.10 ± 0.01	81.47 ± 0.58	401.1 ± 23.2	77.06 ± 4.85

compressive moduli of HP60 and nHP60 could significantly decrease the connecting stability between cells and materials. Therefore, in terms of the need for stable cell culture, materials fabricated with P40 or P50 are ideal candidates for future applications. Considering the mechanical properties, hydrophilicity, degradability, and biocompatibility, HP40 and nHP40 were concluded to be the best candidates for 3D scaffold fabrication.

3.2.3. Printing quality

To further ensure a suitable particle size of HAP for 3D printing, composites containing micro- and nanoparticles were used in the preliminary test of scaffold fabrication. The overall printed structures of both scaffolds were similar, as indicated in Fig. S6. However, large differences were observed in the SEM images obtained at high magnification. In contrast to the smooth surface of nHP40 scaffolds, the surfaces of scaffolds fabricated with HP40 were very rough due to the exposed HAP particles (Fig. 2c–d). Because the diameters of some HAP microparticles were greater than the designed wall thickness, it was inevitable that these microparticles could not be fully encapsulated in the walls, leaving behind the coarse surface. Although rough surfaces were considered beneficial for cell adhesion, a large decrease in cell viability on HP40 scaffolds could occur as the exposed microparticles may fall off from the scaffolds during normal handling, which removes the cells adhered to them as well. In the EDX mapping of calcium element, it was found that the HAP particles on nHP40 scaffolds were more evenly distributed than the ones on HP40 scaffolds. Hence, it was expected that nHP40 could provide more uniform osteoinductive environments for cell culture. Moreover, the microparticles were easily stocked within the pores during fabrication, which significantly lowered the possibility of successful printing. To ensure the integrity of the scaffold and maintain the overall printing quality, nHP40 was selected as the final material for 3D printing.

3.3. Design and characterization of 3D-printed scaffolds

Three types of scaffold designs were proposed to produce BTE scaffolds with nHP40 via DLP-AM. The detailed morphology of the pores was designed into a gyroid, a structural unit with a triply periodic minimal surface, and zero-mean curvature [44]. It is one of the most popular structures in scaffold design owing to its biomimetic shapes [45], good mechanical performance under high porosity [46] and super high permeability for cell infiltration [47]. In addition, the pore sizes were set at 200, 300, and 400 μm for G200, G300, and G400, respectively, which has been suggested as the most suitable range for balancing the permeability and capability of tissue growth [48]. The porosities of scaffolds were all set to 80 % for better comparison in biological evaluations. However, 3D printing through photocuring often leads to larger-than-designed products owing to overcuring. To reach the targeted pore sizes and porosities, a series of trial-and-error processes led to adjustments in digital 3D designs, including pore sizes and wall thicknesses.

Based on the results from adjusted designs shown in Table 2 and Fig. 3a–c, scaffolds were 3D printed and imaged by optical camera and SEM (Fig. 3d–f and Fig. 3g–j). From the optical images, it was

demonstrated that the general morphologies of the printed scaffolds were similar to those of the digital designs, while there were obvious differences in pore sizes and wall thickness compared to the theoretical 3D model, as predicted in the design process. To obtain the experimental size parameters of the printed products, measurements were performed on the bright-field images of the wet samples. As shown in Table 3, the pore sizes were close to the targeted values, while the wall thickness increased, possibly owing to inevitable overcuring. Nevertheless, the porosities of the scaffolds were all approximately 82 % according to the calculations, ensuring approximately equal spaces for cell culture.

The detailed morphology and mechanical properties of the scaffolds were characterized using SEM and compression tests, respectively. As shown in the SEM images, unexpected grating patterns were found on the scaffold surfaces (Fig. 3g–j) due to the limited printing precision in the z-axis because DLP printing operated through layer-by-layer photocuring processes. However, it was expected that such microstructures might be beneficial for cell adhesion, as the width of these gratings was approximately 5–10 μm, which falls within the range for contact guidance for cells [49]. In the mechanical property tests, the stress-strain curves of the scaffolds were recorded, and the compressive modulus was calculated from the linear region of the plot (Fig. 3k). It was then revealed that the moduli of all the scaffolds were similar (Fig. 3l), providing similar conditions for subsequent experiments. These data suggest that the designed gyroid scaffolds were successfully fabricated by 3D printing, confirming the preparation for future biological experiments.

3.4. In-vivo evaluation of bone regeneration efficacy of 3D-printed scaffolds

To characterize in *in-vivo* biocompatibility and osteogenic capability, 3D-printed scaffolds were implanted into critical-sized bone defects in rats (Fig. 4a). G200 and G400 were selected to investigate the influence of the pore size. After surgery, micro-CT was performed on live animals at weeks 4 and 8 to monitor defect recovery. New bone formation was confirmed in both the scaffold groups (Fig. 4b). Subsequent image analyses showed a significantly higher new bone volume ratio for G400 at all time, which reached around 60 % at week 8 (Fig. 4c). The major differences between the two scaffolds in the new bone volume ratio demonstrated the effect of variations in the surface area and permeability. On the other hand, relative bone densities for regenerated tissue were found to be similar in both scaffold groups, suggesting nearly identical progression of mineralization (Fig. 4d).

Calvarial samples were collected and fixed for histological analysis after the rats were euthanized at week 8. The results of H&E staining (Fig. 4e) showed that most of the scaffolds were still intact, indicating a limited degree of degradation within 8 weeks of implantation. In addition, most of the new bone was observed to form on top of the scaffolds, while fibrotic tissues were found inside the porous structures. Minimal immune response was also confirmed by the absence of a fibrous capsule around the scaffolds. In the subsequent validation using Masson's trichrome staining, similar observations were made from the images (Fig. 4f). New bone ratios from histological staining were also analyzed, indicating that 32.54 ± 3.26 % and 66.88 ± 8.79 % of the defected area was regenerated in G200 and G400 groups respectively. Collectively, these results suggested that both scaffolds were effective in stimulating osteogenesis.

With minimal formation of the fibrous capsule, it was expected that most scaffold structures would be covered by soft tissues in the early stage of implantation. The larger surface area of the G200 scaffolds could lead to recruitment of more cells for attachment at this stage. Because the two scaffolds shared the same porosity, each individual pore in the G200 scaffolds was more rapidly filled with tissues. In the work of Guillaume et al., it was shown that the sufficient surface exposure of HAP on scaffolds was effective in promoting osteogenesis [50]. However, despite the higher exposure of nHAP in G200, thus stronger attraction, the poorer permeability led to a lower number of migrated

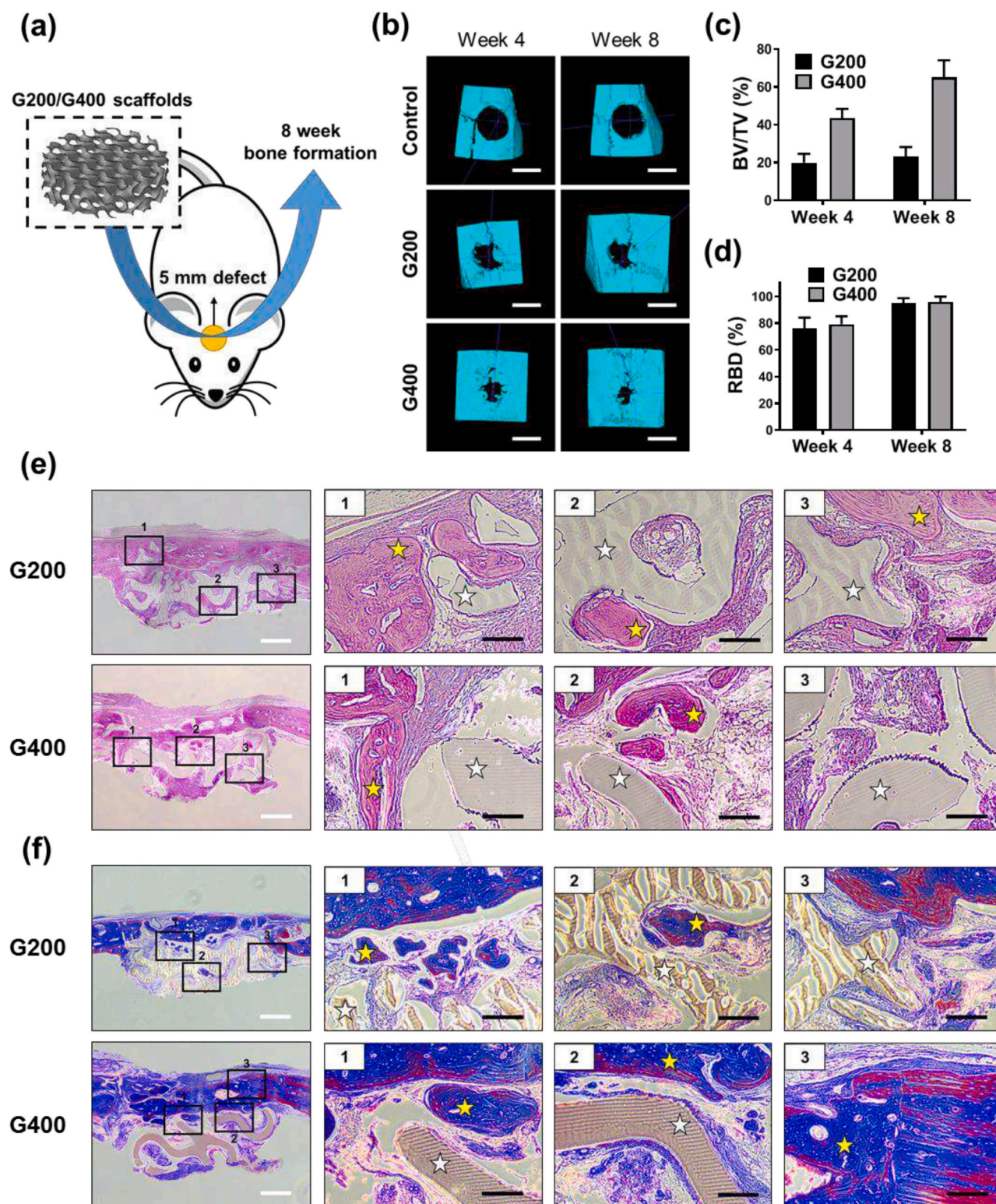


Fig. 4. *In-vivo* bone regeneration with 3D-printed scaffolds: (a) schematic diagram, (b) μ CT images, (c) bone volume to total volume ratio (BV/TV), (d) Relative bone density (RBD), (e) H&E staining results, (f) Masson's trichrome staining results. Scale bar in (b): 4 mm, White scale bars in (e–f): 1 mm, Black scale bars in (e–f): 200 μ m. White stars representing scaffold while yellow stars representing new bone in (e–f).

stem cells, which finally led to less bone regeneration. As the permeability was significantly higher in G400, this phenomenon was less obvious, yet the smaller amount of fibrotic tissue in the pores still impeded complete bone regeneration. To overcome this problem, ECM-based hydrogels containing stem cells have been proposed for several

reasons. First, efficient stem cell delivery into the center of the scaffolds leads to simultaneous local osteogenesis in the pores. Second, the infused hydrogels could act as physical barriers against rapidly proliferating fibroblasts immediately after implantation, leaving more space for new bone formation. Similar anti-fibrosis concepts using hydrogels

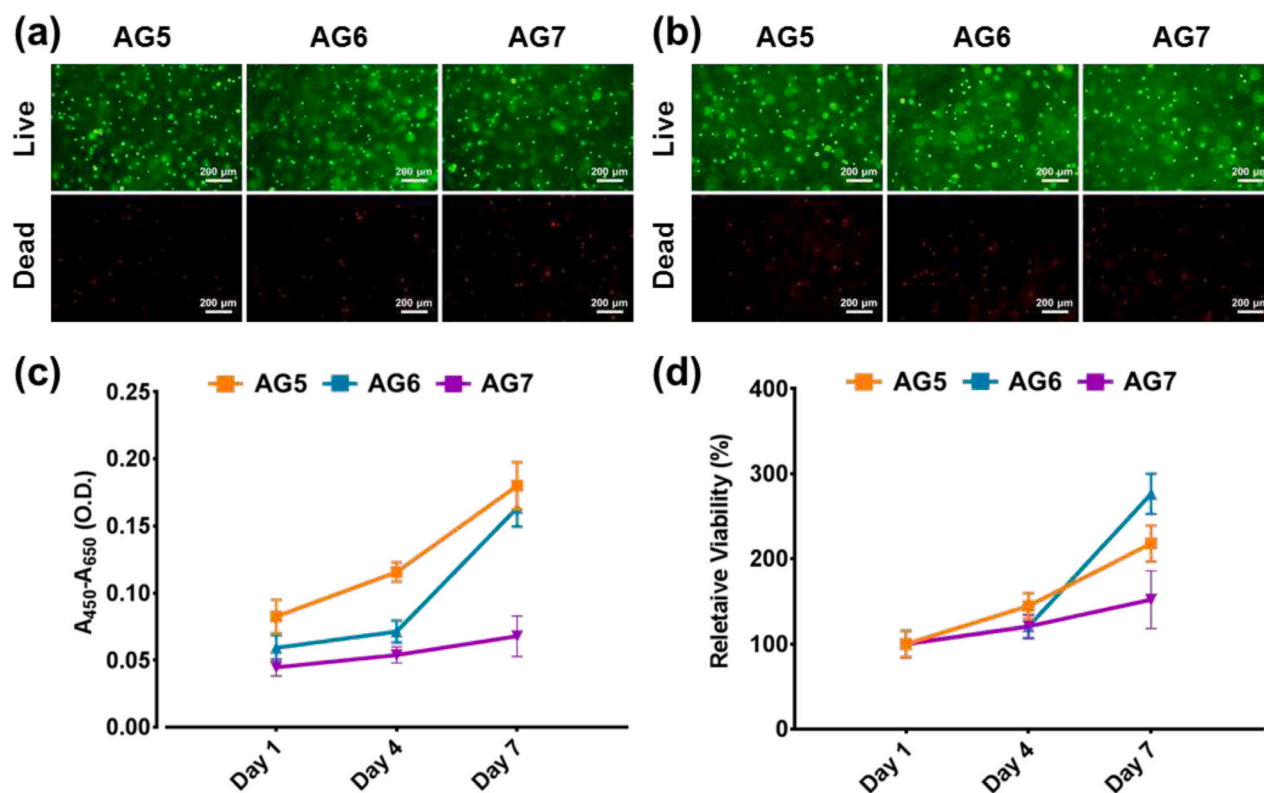


Fig. 5. Biocompatibility tests of Wharton's jelly-derived mesenchymal stem cells (WJMSC) on cell-laden hydrogel: (a–b) live/dead staining ((a) for day 0; (b) for day 1). (c–d) One-week cell viability tests.

were presented by Feng et al. [51]. Finally, hydrogels made with ECM-related proteins further increased the overall biocompatibility of the scaffolds during tissue regeneration. Therefore, in the following sections, cell-laden hydrogels are fabricated, optimized, and combined with 3D-printed scaffolds as hybrid systems for stem cell culture and differentiation.

3.5. Selection of cell-laden hydrogel for hybrid scaffold fabrication

Cell-laden hydrogels were fabricated by mixing gelatin, alginate, and WJMSC, followed by gelation with calcium ions. The alginate concentration was set at 2 %, while the gelatin concentration varied from 5, 6 and 7 % for AG5, AG6, and AG7, respectively. Gelatin, the denatured form of collagen, functions as an ECM-like component in hydrogels; thus, its concentration should be tailored to achieve sufficient biocompatibility. Therefore, the hydrogels were optimized through two types of biocompatibility tests: live/dead staining and long-term proliferation tests. Live/dead staining was conducted to characterize the cell damage caused by the fabrication procedures because cells may die in some of the experimental steps, including hydrogel mixing, cooling, or cross-linking. As shown in Fig. 5a, the number of living cells was significantly larger than the number of dead cells, which ensured safety during hydrogel fabrication. The fluorescent signals in the images were further analyzed to quantify cell viability. All cell viabilities were above 90 %, as indicated in Table S2. Similar results were found in experiments repeatedly performed on cell-laden hydrogels that had been cultured for 1 d (Fig. 5b), confirming that cell viability was well maintained.

To identify the most suitable gel for long-term cell culture, cell-laden hydrogels were cultured for one week and cell viability was quantified. The viability of cells encapsulated in the hydrogels increased throughout the experiment (Fig. 5c), suggesting that the cells could proliferate within the polymer matrix. The viability results of AG7 on day 7 were

clearly lower than those of the others, while no significant differences were observed on the same day between AG5 and AG6. In addition, the average viability results of AG5 at each time point were always above those of AG6, whereas similar conditions were also observed between AG6 and AG7. However, as previously indicated, the viability results on day 1 should be roughly the same for all hydrogels because the number of live cells was quite similar according to live/dead staining. Other factors, rather than native biocompatibility, may exist in the experiments, leading to this phenomenon. The difference in the diffusion efficiency of the viability test reagent is the most significant factor. The WST-8 molecules in the CCK-8 assay were only reduced once they diffused across the hydrogel and contacted cells. Since the diffusion efficiency was highly dependent on the solute concentration within the hydrogel, it was expected that gels with relatively lower concentrations of gelatin, such as AG5, would allow more efficient diffusion of the viability reagents, resulting in more WST-8 reduction.

To better compare the cell proliferation capacity without diffusion issues, the viability results at days 4 and 7 were normalized with the data at day 1 for each individual group, representing the relative viabilities within 7 days (Fig. 5d). The cell proliferation results of AG6 on day 7 were the highest among all the experimental groups. Generally, cell proliferation is positively correlated with gelatin concentration, as gelatin is commonly added to increase the biocompatibility of alginate hydrogels [52]. The unexpected proliferation trends may be due to differences in diffusion efficiency. The oxygen and nutrient diffusion coefficients in cell-laden hydrogels are negatively correlated with polymer concentration [53]. With more gelatin added to the hydrogels, the density of the bulk matrix increased, so less nutrients and oxygen could diffuse into the cells, leading to slower proliferation. It was hypothesized that the outstanding viability of AG6 on day 7 was a result of balanced biocompatibility and nutrient diffusion. Consequently, AG6 was chosen as the cell-laden hydrogel to generate hybrid systems for

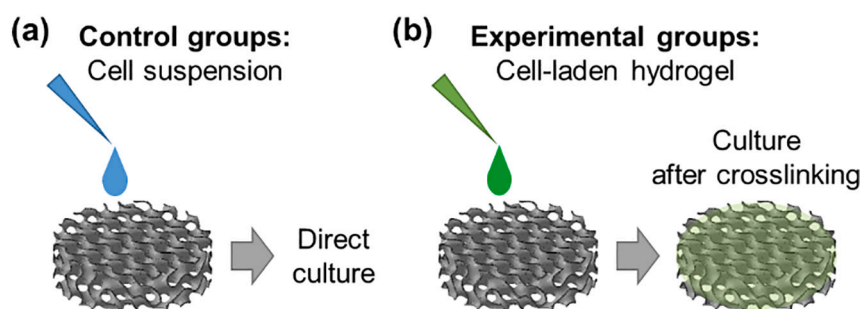


Fig. 6. Schematic diagram of the preparation for *in-vitro* study on hybrid scaffolds: (a) Control groups with direct cell seeding, (b) experimental groups with cell seeding by hydrogels.

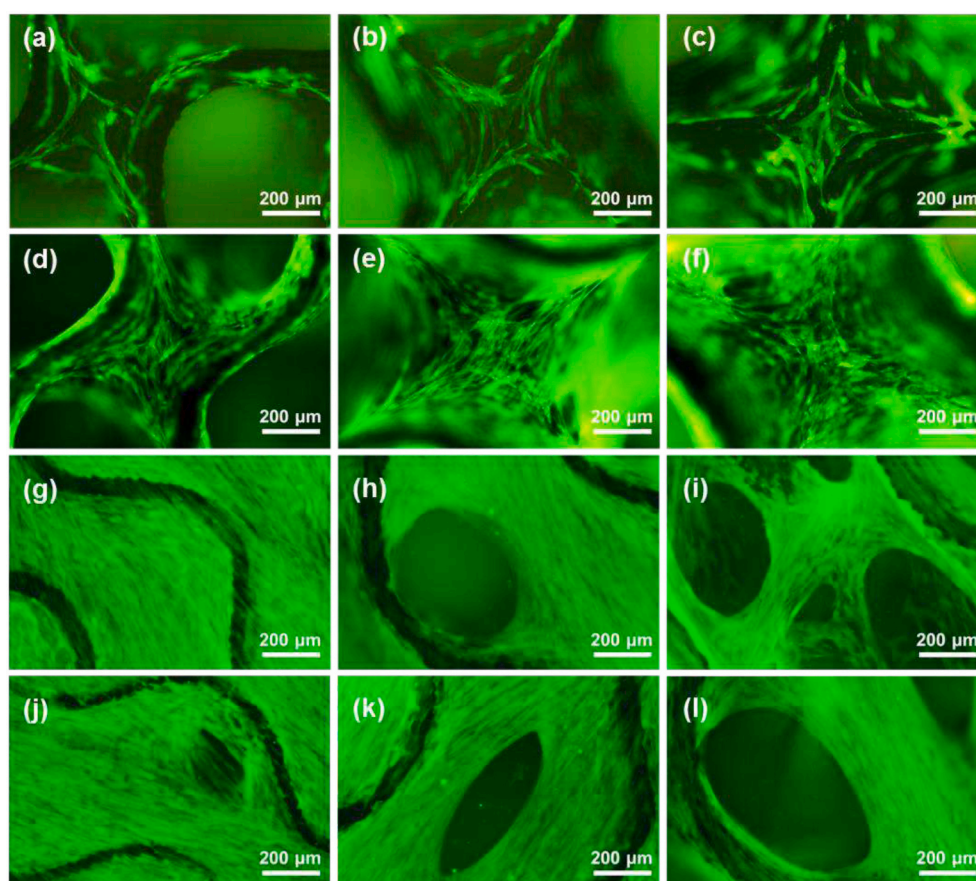


Fig. 7. Live cell imaging of G200 (a, d, g, j), G300 (b, e, h, k) and G400 (c, f, i, l) at day 1 (a–c), 7 (d–f), 14 (g–i) and 21 (j–l).

further applications.

3.6. *In-vitro* culture of WJMSC on hybrid scaffolds

Hybrid scaffolds were produced by the integration of AG6 into the scaffolds (Fig. 6b). To evaluate the advantages of hybrid scaffolds on cell viability, the constructs were cultured for 3 weeks, and live cell imaging was conducted to confirm cell morphology and distribution. It was shown that cells in the control groups, which were prepared by direct seeding with cell suspension (Fig. 6a), were evenly distributed on the scaffolds at day 1 (Fig. 7a–c), and then reached confluency at day 7 (Fig. 7d–f). Afterwards, the cells formed clusters across the scaffold pores on day 14 (Fig. 7g–i) and day 21 (Fig. 7j–l). It was observed that the efficiency of the cells to cover the pores was negatively correlated with pore sizes (Fig. 7j–l), which fits the hypothesis made in the previous

animal work section. Such phenomena can be explained by two factors: the surface area of the scaffolds and the cell number required for cluster formation. The surface area of the scaffolds with smaller pore sizes was larger, which meant that there were more starting areas for cluster formation. Meanwhile, the cell number required for the smaller pores to cross the structures was much less than that required for the larger pores, which further reduced the time required. On the other hand, a delayed seeding process on the scaffolds was observed in the experimental groups. Cells delivered by AG6 were considered to remain within the gels at day 1 (Fig. 8a–c) because of their spherical shape. It was until day 7 that the cells started to adhere to the scaffolds, while some cells were still within the hydrogels (Fig. 8d–f). At day 14, fewer cells were observed in the encapsulated form (Fig. 8g–i). Similar cell clusters were observed in the control groups, which formed around the pores and fully covered most of the pores on day 21 (Fig. 8j–l). Compared with the

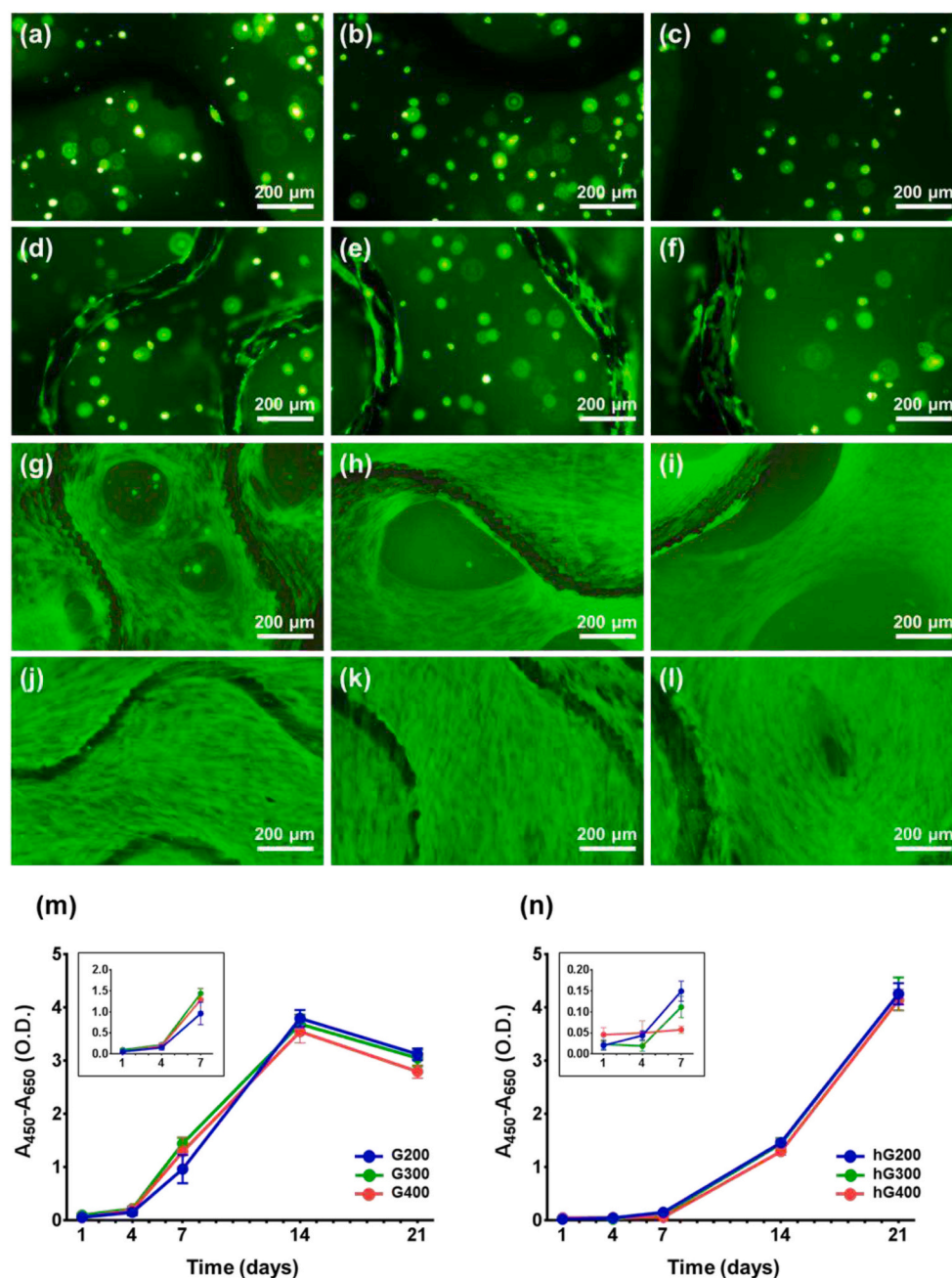


Fig. 8. Biocompatibility tests of hybrid scaffolds: (a–l) Live cell imaging of hG200 (a, d, g, j), hG300 (b, e, h, k) and hG400 (c, f, i, l) at day 1 (a–c), 7 (d–f), 14 (g–i) and 21 (j–l). (m–n) Cell viability tests of scaffold only (m) and hybrid scaffolds (n).

control groups, cells initially delivered by hydrogels covered pores with a greater area at the end of the experiments, suggesting that gel-assisted seeding led to more stable cell cluster formation. Moreover, the hydrogel remaining in the first week could act as a barrier against soft-tissue penetration in clinical applications, as mentioned above. It was then suggested that cell seeding with hydrogels is more beneficial than the traditional methods.

To compare cell viabilities under different seeding methods, the CCK-8 assay was performed throughout the culture processes (Fig. 8m–n). The cell viabilities of the control groups increased rapidly from day 4 to day 14 but eventually decreased at day 21. In addition, there were no obvious differences in cell proliferation between scaffolds with different pore sizes (Fig. 8m). In contrast, cells initially seeded with hydrogels started fast proliferation from day 7 to day 21, and the viabilities were all maintained at the last time point (Fig. 8n). As for the

comparison between the scaffolds in the experimental groups, the proliferation trends of all gel scaffolds were shown to be similar without significant differences. Therefore, it could be concluded that the cell seeding method affected cell viability, whereas pore sizes seemed to have little effect on both the control and experimental groups.

To explain the different proliferation trends between the two seeding methods, it was hypothesized that the time point of cells in contact with scaffold surfaces played an important role, which was supported by the imaging results. In the control groups, cells immediately interacted with the polymer after seeding and grew in a 2-D manner in the first 4 days, followed by the formation of multiple cell layers until day 14 (Fig. 7a–i). A possible reason for the decreased viability at day 21 was that the cell clusters formed too fast on the surfaces, which caused hypoxia or even necrosis due to a lack of oxygen and nutrients inside the pores. Studies have shown that cells in the center of solid clusters with diameters >500

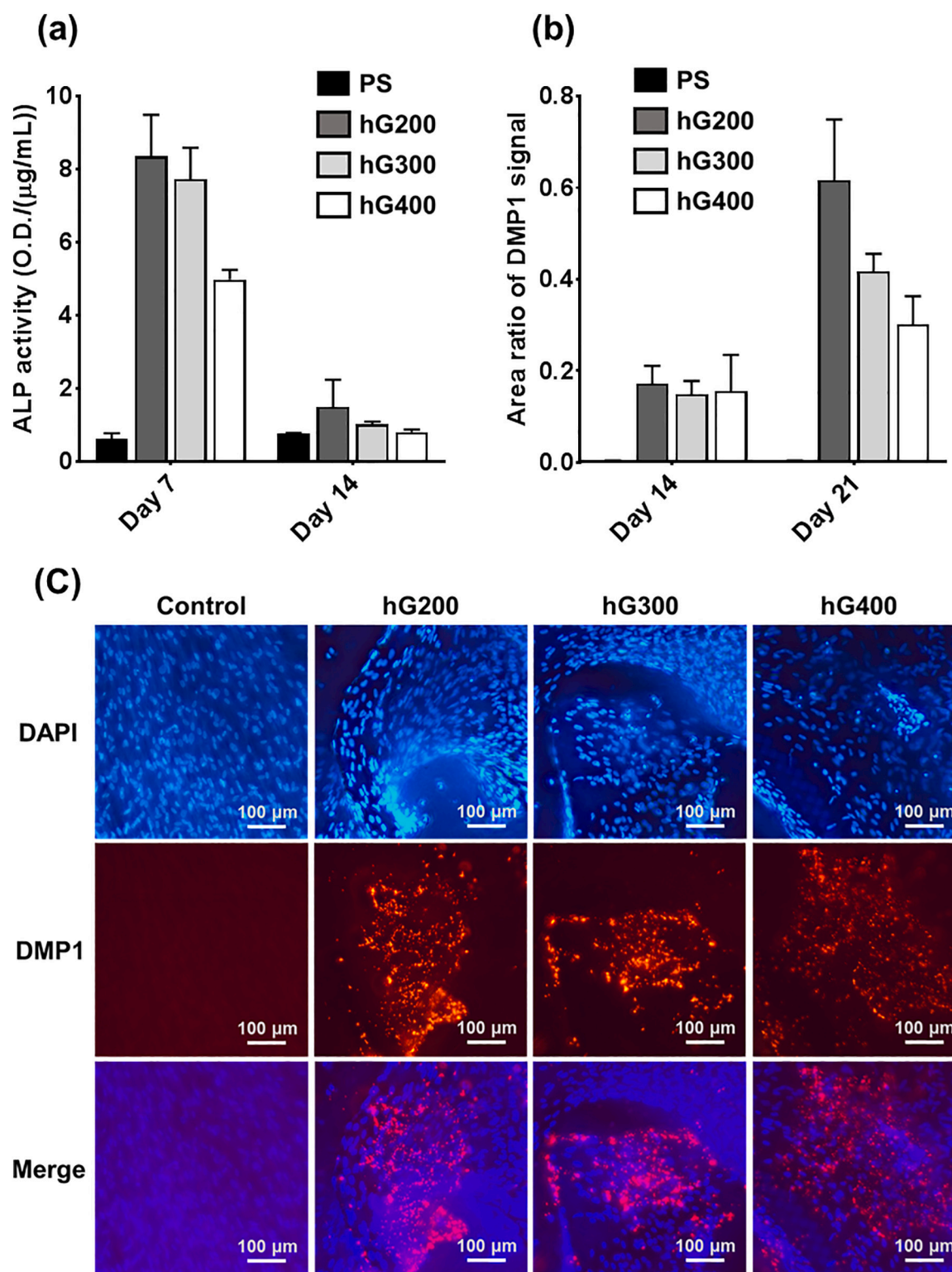


Fig. 9. Evaluation of osteogenic differentiation on hybrid scaffolds: (a) ALP activity assay. (b) Quantification of DMP1 IHC staining. (c) DMP1 IHC staining results at day 21.

μm cannot survive [54]. In contrast, cells encapsulated in the hydrogels proliferated slowly during the first week, implying that most cells did not adhere to the scaffold surfaces. This explanation is consistent with the live cell images taken on day 1 (Fig. 8a–c). As shown in the blown up illustration in Fig. 8n, it was hypothesized that some cells in hG200 and hG300 began to contact the scaffolds at day 4, while similar situations for hG400 were found at day 7. After cell adhesion, as demonstrated in

Fig. 8d–f, the overall proliferation trends resembled those of the control groups, which was mostly contributed by the cell growth on polymer composites. Although the delayed cell adhesion in the hybrid scaffolds led to slightly slower proliferation, it could possibly be the key to forming cell clusters with fewer diffusion issues. Considering the stability of the cell clusters after long-term culture, hybrid scaffolds were chosen over scaffolds with direct seeding for future studies.

3.7. *In-vitro* osteogenic differentiation on hybrid scaffolds

In BTE, scaffolds could either be directly implanted into defect sites to facilitate regeneration or served as platforms for *in-vitro* bone formation. Bone constructs produced *in-vitro* could be applied as transplantable grafts or disease models for drug screening. Therefore, scaffolds capable of stimulating osteogenesis *in-vitro* were considered to hold great potential in various BTE applications. To further identify the most suitable hybrid scaffold design for BTE, differentiation tests were performed to evaluate osteogenesis progression. In the early stages of osteogenic differentiation, alkaline phosphatase (ALP) is the most well-known marker for its high expression in osteoblasts. During bone regeneration, ALP is secreted to maintain the phosphate concentration necessary for mineralization [55]. Therefore, the enzymatic activity of ALP per DNA unit was measured for samples collected on days 7 and 14, which is the time required for osteoblast formation under osteogenic conditions [56]. As indicated in Fig. 9a, the ALP activities of all scaffold designs were higher than those of the control groups on day 7, proving the osteoinduction ability of the hybrid scaffolds. It was also shown that the efficiency of the stimulation was negatively correlated with the pore size, as the data for G400 were significantly lower than those for the other two designs. Differences in the surface exposure of HAP may be the reason for the smallest surface area of G400. At day 14, it was observed that all ALP activities of the experimental groups decreased dramatically, which could possibly be attributed to the change in cell numbers and cell states. It was found that cells in hybrid scaffolds started to proliferate rapidly from day 7 to day 14, as indicated by viability tests. The increase in stem cell numbers may be faster than the increase in osteoblast populations, supported by the fact that the cell proliferation rate usually slows down with the progression of differentiation [57]. The average ALP activity then decreased owing to the large increase in DNA content. Another possibility is that late-stage osteogenesis may have already occurred on day 14. ALP expression was largely decreased in mature osteocytes, which are usually formed after cultured 2–3 weeks *in vitro* with osteogenic factors. Studies have shown that weaker ALP activity at around week 2–3 correlated with an increased population of mature osteocytes [58]. Therefore, late-stage osteogenesis was characterized to test this hypothesis.

Immunostaining of dentin matrix protein 1 (DMP1) was applied to the hybrid scaffolds cultured for 2 and 3 weeks to evaluate osteocyte formation. DMP1 is an acidic phosphoprotein that is specifically expressed in mature bone tissues and plays an important role in bone mineralization [59]. As shown by the fluorescence signals and subsequent imaging quantifications, late-stage osteogenesis occurred on all hybrid scaffolds but not on the control groups at day 14 (Fig. S7, Fig. 9b–c). In addition, the area ratio for the DMP1 signals increased after another week of culture. No significant differences between each design were observed on day 14, whereas a negative correlation between pore size and DMP1 expression was confirmed on day 21. Since the trend resembled that seen in the ALP activity assay at day 7, the possible reason may be similar, which was related to HAP exposure, as discussed above. The hG200 scaffold was then considered the design with the best performance for stem cell proliferation and differentiation. However, it should also be noted that even with a weaker osteoinductive effect for the other two designs, they still provided favorable environments for osteogenesis without the addition of external growth factors. In practical applications, the scaffolds can be designed into larger and more complex shapes, whereas the pore sizes may be re-selected according to each clinical requirement to maximize healing efficacy. Nevertheless, these biological tests collectively proved the potential of the hybrid scaffold design for BTE. Further development should be conducted to extend the feasibility of hybrid systems in clinical applications, as the scaffold sizes are still far from those of human bone defects. For example, improving diffusion in scaffolds by integrating the vasculature system could be beneficial for reconstructing large-sized defects. The preculture of hybrid scaffolds under external forces in

bioreactors should also be considered as stem cells that can undergo more efficient osteogenic differentiation under these conditions [60].

4. Conclusion

In this study, we developed a hybrid scaffold design containing osteoinductive 3D scaffolds and bioactive hydrogels for BTE applications. A novel biodegradable polymer PEGSA was successfully synthesized and combined with HAP particles to generate a series of polymer composites. Through physical and biological characterization, nHP40 was selected as the resin for 3D-printing. Three types of gyroid scaffolds with well-controlled pore sizes and morphologies were fabricated using DLP-AM. In subsequent *in-vivo* evaluations, 3D-printed scaffolds were confirmed to promote osteogenesis; however, limitations were also found, which led to the need for hydrogel incorporation. Bioactive hydrogels were fabricated, optimized, and integrated with 3D-printed products to generate hybrid scaffolds. These designs have been proven to be more beneficial in cell culture than direct seeding processes, and are also capable of stimulating osteogenic differentiation *in vitro*. In conclusion, the proposed hybrid scaffold design provides a promising strategy for cell culture and delivery in BTE.

CRediT authorship contribution statement

Yi-Ting Chen: Conceptualization, Methodology, Validation, Software, Formal analysis, Investigation, Data curation, Writing – original draft, Writing – review & editing, Visualization, Supervision. **Ya-Han Chuang:** Conceptualization, Methodology, Software, Formal analysis, Validation, Writing – review & editing. **Chao-Ming Chen:** Conceptualization, Methodology, Resources. **Jir-You Wang:** Conceptualization, Methodology, Resources. **Jane Wang:** Conceptualization, Resources, Writing – review & editing, Funding acquisition, Project administration.

Declaration of competing interest

The authors declare that they have no known competing financial interests or personal relationships that could have appeared to influence the work reported in this paper.

Data availability

The authors do not have permission to share data.

Acknowledgements

Funding for this work was provided by the Ministry of Science and Technology (Taiwan), National Health Research Institute (Taiwan), and VGHUST Joint Research Program (Taiwan) under contract of MOST 111-2221-E-007-026-MY2, MOST 112-2622-8-007-007, NHRI-EX111-10812EC, and VGHUST110-G6-1-1.

Appendix A. Supplementary data

Supplementary data to this article can be found online at <https://doi.org/10.1016/j.bioadv.2023.213562>.

References

- [1] A.R. Amini, C.T. Laurencin, S.P. Nukavarapu, Bone tissue engineering: recent advances and challenges, *Crit. Rev. Biomed. Eng.* 40 (5) (2012) 363–408.
- [2] N. Sultana, M. Wang, PHBV/PLLA-based composite scaffolds fabricated using an emulsion freezing/freeze-drying technique for bone tissue engineering: surface modification and *in vitro* biological evaluation, *Biofabrication* 4 (1) (2012), 015003.
- [3] J.Q. Song, et al., Assembling of electrospun meshes into three-dimensional porous scaffolds for bone repair, *Biofabrication* 9 (1) (2017).

- [4] S.P. Parthiban, et al., BoneMA-synthesis and characterization of a methacrylated bone-derived hydrogel for bioprinting of in-vitro vascularized tissue constructs, *Biofabrication* 13 (3) (2021).
- [5] M. Castilho, et al., Direct 3D powder printing of biphasic calcium phosphate scaffolds for substitution of complex bone defects, *Biofabrication* 6 (1) (2014), 015006.
- [6] N. Sears, et al., Fabrication of biomimetic bone grafts with multi-material 3D printing, *Biofabrication* 9 (2) (2017), 025020.
- [7] H. Zhuang, et al., 3D-printed bioceramic scaffolds with Fe₃S₄ microflowers for magnetothermal and chemodynamic therapy of bone tumor and regeneration of bone defects, *Biofabrication* 13 (4) (2021).
- [8] N.P. Macdonald, et al., Comparing microfluidic performance of three-dimensional (3D) printing platforms, *Anal. Chem.* 89 (7) (2017) 3858–3866.
- [9] R. Colella, F.P. Chietera, L. Catarinucci, Analysis of FDM and DLP 3D-printing technologies to prototype electromagnetic devices for RFID applications, *Sensors* 21 (3) (2021).
- [10] K.S. Lim, et al., Bio-resin for high resolution lithography-based biofabrication of complex cell-laden constructs, *Biofabrication* 10 (3) (2018).
- [11] Y.H. Wei, et al., Stereolithography-based additive manufacturing of high performance osteoinductive calcium phosphate ceramics by a digital light-processing system, *ACS Biomater. Sci. Eng.* 6 (3) (2020) 1787–1797.
- [12] D. Dean, et al., The calibration of continuous Digital Light Processing (cDLP) for the highly accurate additive manufacturing of tissue engineered bone scaffolds, *Innov. Dev. Virt. Phys. Prototyp.* (2012) 57–66.
- [13] C.L. Teng, et al., Design of photocurable, biodegradable scaffolds for liver lobule regeneration via digital light process-additive manufacturing, *Biofabrication* 12 (3) (2020).
- [14] C.F. Bellani, et al., Sutureable elastomeric tubular grafts with patterned porosity for rapid vascularization of 3D constructs, *Biofabrication* 13 (3) (2021).
- [15] B. Liang, et al., Poly (glycerol sebacate)-based bio-artificial multiporous matrix for bone regeneration, *Front. Chem.* (2020) 8.
- [16] S.H. Zaky, et al., Poly (glycerol sebacate) elastomer supports osteogenic phenotype for bone engineering applications, *Biomed. Mater.* 9 (2) (2014).
- [17] S.H. Zaky, et al., Poly(glycerol sebacate) elastomer: a novel material for mechanically loaded bone regeneration, *Tissue Eng. A* 20 (1–2) (2014) 45–53.
- [18] S.H. Zaky, et al., Poly (glycerol sebacate) elastomer supports bone regeneration by its mechanical properties being closer to osteoid tissue rather than to mature bone, *Acta Biomater.* 54 (2017) 95–106.
- [19] M. Rostamian, et al., Design and characterization of poly(glycerol-sebacate)-co-poly (caprolactone) (PGS-co-PCL) and its nanocomposites as novel biomaterials: the promising candidate for soft tissue engineering, *Eur. Polym. J.* 138 (2020).
- [20] J. Hu, et al., Electrospinning of poly(glycerol sebacate)-based nanofibers for nerve tissue engineering, *Mater. Sci. Eng. C Mater. Biol. Appl.* 70 (2017) 1089–1094.
- [21] A. Patel, et al., Highly elastomeric poly(glycerol sebacate)-co-poly(ethylene glycol) amphiphilic block copolymers, *Biomaterials* 34 (16) (2013) 3970–3983.
- [22] Y.F. Ma, et al., PEGylated poly(glycerol sebacate)-modified calcium phosphate scaffolds with desirable mechanical behavior and enhanced osteogenic capacity, *Acta Biomater.* 44 (2016) 110–124.
- [23] Z.Y. Qiu, et al., Mineralized collagen: rationale, current status, and clinical applications, *Materials* 8 (8) (2015) 4733–4750.
- [24] H. Zhou, J. Lee, Nanoscale hydroxyapatite particles for bone tissue engineering, *Acta Biomater.* 7 (7) (2011) 2769–2781.
- [25] M.J. Lee, et al., Effect of hydroxyapatite on bone integration in a rabbit tibial defect model, *Clin. Orthop. Surg.* 2 (2) (2010) 90–97.
- [26] G. Turnbull, et al., 3D bioactive composite scaffolds for bone tissue engineering, *Bioact. Mater.* 3 (3) (2018) 278–314.
- [27] M. Zhang, et al., Polydopamine regulated hydroxyapatite microspheres grown in the three-dimensional honeycomb-like mollusk shell-derived organic template for osteogenesis, *Biofabrication* 12 (3) (2020), 035022.
- [28] C. Zhou, et al., Biomimetic fabrication of a three-level hierarchical calcium phosphate/collagen/hydroxyapatite scaffold for bone tissue engineering, *Biofabrication* 6 (3) (2014), 035013.
- [29] C.M. Hwang, et al., Fabrication of three-dimensional porous cell-laden hydrogel for tissue engineering, *Biofabrication* 2 (3) (2010), 035003.
- [30] W. Kim, G.H. Kim, Highly bioactive cell-laden hydrogel constructs bioprinted using an emulsion bioink for tissue engineering applications, *Biofabrication* 14 (4) (2022).
- [31] F. Ghorbani, et al., Bioprinting a cell-laden matrix for bone regeneration: a focused review, *J. Appl. Polym. Sci.* 138 (8) (2021).
- [32] Y.X. Luo, et al., 3D printing of concentrated alginate/gelatin scaffolds with homogeneous nano apatite coating for bone tissue engineering, *Mater. Des.* 146 (2018) 12–19.
- [33] O.A. Hamid, et al., 3D bioprinting of a stem cell-laden, multi-material tubular composite: an approach for spinal cord repair, *Mater. Sci. Eng. C Mater. Biol. Appl.* 120 (2021), 111707.
- [34] L. Dong, et al., 3D-printed poly(epsilon-caprolactone) scaffold integrated with cell-laden chitosan hydrogels for bone tissue engineering, *Sci. Rep.* (2017) 7.
- [35] M.I. Bogachev, et al., Fast and simple tool for the quantification of biofilm-embedded cells sub-populations from fluorescent microscopic images, *PLoS One* 13 (5) (2018), e0193267.
- [36] D. Aronov, et al., Tunable hydroxyapatite wettability: effect on adhesion of biological molecules, *Process Biochem.* 41 (12) (2006) 2367–2372.
- [37] B. Zhang, et al., Multifunctional scaffolds for facile implantation, spontaneous fixation, and accelerated long bone regeneration in rodents, *Sci. Transl. Med.* 11 (502) (2019).
- [38] W.J. Hadden, et al., Stem cell migration and mechanotransduction on linear stiffness gradient hydrogels, *Proc. Natl. Acad. Sci. U. S. A.* 114 (22) (2017) 5647–5652.
- [39] Y. Tamada, Y. Ikada, Cell-adhesion to plasma-treated polymer surfaces, *Polymer* 34 (10) (1993) 2208–2212.
- [40] A.S. Ansari, et al., Osteogenic induction of Wharton's jelly-derived mesenchymal stem cell for bone regeneration: a systematic review, *Stem Cells Int.* 2018 (2018) 2406462.
- [41] M.L. Weiss, D.L. Troyer, Stem cells in the umbilical cord, *Stem Cell Rev.* 2 (2) (2006) 155–162.
- [42] ISO, Biological Evaluation of Medical Devices. Part 5: Tests for In Vitro Cytotoxicity, International Standards Organisation, 2009.
- [43] M.Y. Sun, et al., Effects of matrix stiffness on the morphology, adhesion, proliferation and osteogenic differentiation of mesenchymal stem cells, *Int. J. Med. Sci.* 15 (3) (2018) 257–268.
- [44] R. Tino, et al., Gyroid structures for 3D-printed heterogeneous radiotherapy phantoms, *Phys. Med. Biol.* 64 (21) (2019).
- [45] J.G. Torres-Rendon, et al., Bioactive gyroid scaffolds formed by sacrificial templating of nanocellulose and nanochitin hydrogels as instructive platforms for biomimetic tissue engineering, *Adv. Mater.* 27 (19) (2015) 2989–2995.
- [46] D.W. Abueidda, et al., Mechanical properties of 3D printed polymeric gyroid cellular structures: experimental and finite element study, *Mater. Des.* 165 (2019).
- [47] F.P.W. Melchels, et al., Effects of the architecture of tissue engineering scaffolds on cell seeding and culturing, *Acta Biomater.* 6 (11) (2010) 4208–4217.
- [48] V. Karageorgiou, D. Kaplan, Porosity of 3D biomaterial scaffolds and osteogenesis, *Biomaterials* 26 (27) (2005) 5474–5491.
- [49] Y.K. Hsieh, et al., Laser-pattern induced contact guidance in biodegradable microfluidic channels for vasculature regeneration, *J. Mater. Chem. B* 6 (22) (2018) 3684–3691.
- [50] O. Guillaume, et al., Surface-enrichment with hydroxyapatite nanoparticles in stereolithography-fabricated composite polymer scaffolds promotes bone repair, *Acta Biomater.* 54 (2017) 386–398.
- [51] M. Feng, et al., Bioprinting of a blue light-cross-linked biodegradable hydrogel encapsulating amniotic mesenchymal stem cells for intrauterine adhesion prevention, *ACS Omega* 6 (36) (2021) 23067–23075.
- [52] R. Yao, et al., Alginate and alginate/gelatin microspheres for human adipose-derived stem cell encapsulation and differentiation, *Biofabrication* 4 (2) (2012).
- [53] L. Figueiredo, et al., Assessing glucose and oxygen diffusion in hydrogels for the rational design of 3D stem cell scaffolds in regenerative medicine, *J. Tissue Eng. Regen. Med.* 12 (5) (2018) 1238–1246.
- [54] S. Daster, et al., Induction of hypoxia and necrosis in multicellular tumor spheroids is associated with resistance to chemotherapy treatment, *Oncotarget* 8 (1) (2017) 1725–1736.
- [55] S. Vimalraj, Alkaline phosphatase: structure, expression and its function in bone mineralization, *Gene* 754 (2020).
- [56] E.K. Moiola, L. Hong, J.J. Mao, Inhibition of osteogenic differentiation of human mesenchymal stem cells, *Wound Repair Regen.* 15 (3) (2007) 413–421.
- [57] S. Ruijtenberg, S. van den Heuvel, Coordinating cell proliferation and differentiation: antagonism between cell cycle regulators and cell type-specific gene expression, *Cell Cycle* 15 (2) (2016) 196–212.
- [58] E.K. Ko, et al., In vitro osteogenic differentiation of human mesenchymal stem cells and in vivo bone formation in composite nanofiber meshes, *Tissue Eng. A* 14 (12) (2008) 2105–2119.
- [59] C. Qin, R. D'Souza, J.Q. Feng, Dentin matrix protein 1 (DMP1): new and important roles for biomineralization and phosphate homeostasis, *J. Dent. Res.* 86 (12) (2007) 1134–1141.
- [60] M.C. Qi, et al., Mechanical strain induces osteogenic differentiation: Cbfa1 and Ets-1 expression in stretched rat mesenchymal stem cells, *Int. J. Oral Maxillofac. Surg.* 37 (5) (2008) 453–458.